

## Full length article

# A decohesion pathway for hydrogen embrittlement in nickel: Mechanism and quantitative prediction

A. Tehranchi<sup>a,\*</sup>, X. Zhou<sup>b</sup>, W.A. Curtin<sup>b</sup><sup>a</sup> Max-Planck-Institut für Eisenforschung GmbH, D-40237 Düsseldorf, Germany<sup>b</sup> Laboratory for Multiscale Mechanics Modeling, EPFL, CH-1015 Lausanne, Switzerland

## ARTICLE INFO

## Article history:

Received 5 April 2019

Revised 26 November 2019

Accepted 26 November 2019

Available online 29 November 2019

## Keywords:

Hydrogen embrittlement

Local diffusion

Nanohydride

Crack

## ABSTRACT

Hydrogen embrittlement (HE) is a ubiquitous and catastrophic mode of fracture in metals. Here, embrittlement is considered as an intrinsic ductile-brittle transition at the crack tip, where H at the crack tip can reduce the stress intensity  $K_{Ic}$  for cleavage below the value  $K_{Ie}$  required for ductile dislocation emission and blunting. Specifically, cleavage fracture along (111) planes in Ni occurs due to the formation of just 3 planar layers of H interstitial occupation at a sharp crack tip. During the cleavage process, the sub-surface H in the upper and lower layers can rapidly diffuse to the fracture surface, lowering the net fracture free energy to  $K_{Ic} < K_{Ie}$  and enabling brittle fracture. Details of the process are demonstrated using both first-principles density functional theory and a new interatomic potential for Ni-H. Thermodynamic and kinetic models show that the 3 layers of H can form at the crack tip in equilibrium at room temperature with bulk H concentrations and loading rates where H embrittlement in Ni is observed. The kinetic model also predicts the slow crack growth rate in agreement with experiments. The energetics of the mechanism is then shown to apply to cleavage along grain boundaries. All together, these results show that a version of “Hydrogen enhanced decohesion” is the operative embrittlement mechanism in Ni.

© 2019 Acta Materialia Inc. Published by Elsevier Ltd. All rights reserved.

## 1. Introduction

During both production and usage, metals are prone to the ingress of hydrogen and, consequently, a severe decrease in mechanical performance. The most persistent mode of failure is a significant loss of ductility accompanied by cleavage-like fracture associated with sharp cracks [1–5]. While known for more than 140 years [6], the underlying physical mechanisms remain a topic of intense scientific debate. Generally, for a given material, H embrittlement depends on H concentration, temperature, and time or loading rate. These observations imply a confluence of mechanical, thermodynamic, and kinetic features that must be captured by any realistic model for H embrittlement.

Existing concepts for hydrogen embrittlement fall into a few categories. The hydrogen enhanced decohesion (HEDE) concept envisions that the presence of H atoms can reduce the fracture energies of material interfaces and make brittle cleavage easier [7–12]. However, it is not sufficient to simply lower the fracture energy. Metals are ductile in part because they are *intrinsically* duc-

tile - a sharp crack will emit dislocations and blunt at load levels far below those at which cleavage fracture can occur. Existing computations of the reduction in fracture surface energy due to hydrogen at realistic hydrogen concentrations are not sufficient to prevent emission and blunting [13,14]. The observation of localized slip bands and extensive dislocation plasticity below the fracture surfaces in hydrogen-charged metals [15,16] has motivated the concept of hydrogen enhanced localized plasticity (HELP) [17–19]. HELP envisions that H atoms enhance plastic activity by reducing dislocation interactions or increasing dislocation mobility or screening defect/dislocation interactions in hydrogen-rich regions. A related concept is the “defactant” concept wherein equilibrium H accumulation at dislocations, under conditions of constant chemical potential, reduces the dislocation line tension, reducing strengthening mechanisms and reducing dislocation nucleation barriers. The connections to the onset of cleavage fracture remains unclear, however. A third concept involves hydrogen-enhanced vacancy formation (HEVF) [20] motivated by observation of nanovoids along the fracture surfaces in nickel [21,22] and iron [23]. Vacancy-hydrogen complexes can be energetically favorable [24,25] but H diffusion and aggregation into voids at grain boundaries, and resulting fracture, are not yet clearly established [26]. Most analyses of the above concepts do not address all the

\* Corresponding author.

E-mail address: [tehranchi@mpie.de](mailto:tehranchi@mpie.de) (A. Tehranchi).

required features: fracture, mechanics, thermodynamics, and kinetics. A fourth concept including these all these features is the inverse of HEDE, where hydrogen aggregation near a sharp crack inhibits dislocation emission, maintaining a sharp crack and leaving cleavage as the only energy-reducing crack tip mechanism [27,28]. Predictions are in good agreement with experiments on ferritic steels but this concept is not yet accepted. [29,30]. Here, we demonstrate that a new nanoscopically-validated version of HEDE operates to embrittle Nickel.

This paper is organized as follows. The mechanism of embrittlement is described and validated in Section 2. The thermodynamics of aggregation of H at the crack tip necessary for the embrittlement and the kinetics of slow crack growth during embrittlement are analyzed in Section 3. Section 4 provides a preliminary extension of the mechanism to embrittlement along grain boundaries. Section 5 discusses the new mechanism in the context of previous embrittlement concepts and points toward future applications of the mechanism beyond Ni.

## 2. H embrittlement analysis and results

### 2.1. Embrittlement: a ductile to brittle transition

Here, we present and validate a new nanoscopically-validated version of HEDE that operates to embrittle Nickel. The analysis addresses the nanoscale conditions at a sharp crack tip in terms of the local stress intensity factor  $K_I$  at the tip. This local  $K_I$  is not equal to the global applied  $K_I^{\text{app}}$ . The latter includes the extensive plastic dissipation in the large plastic zone around the crack and so is always much larger than the local  $K_I$ . But it is the local  $K_I$  that determines the crack tip behavior. There are then two key crack tip quantities. The first quantity is the (local) critical stress intensity for cleavage [31]  $K_{Ic} = \sqrt{\alpha(\mathbf{C})\gamma^{\text{fr}}}$  where  $\gamma^{\text{fr}}$  is the fracture free energy and  $\alpha(\mathbf{C})$  is an elasticity parameter computed using anisotropic linear elasticity in terms of the elastic stiffness tensor  $\mathbf{C}$ . The second quantity is the (local) stress intensity for dislocation emission [32],  $K_{Ie} = \sqrt{\beta(\theta, \phi, \mathbf{C})\gamma_{\text{usf}}}$  where  $\gamma_{\text{usf}}$  is the unstable stacking fault free energy along the slip plane of emission. Here,  $\beta(\theta, \phi, \mathbf{C})$  is an elasticity parameter depending on the slip plane angle  $\theta$  with respect to the crack plane and the angle  $\phi$  of the dislocation Burgers vector with respect to the slip direction. A new theory that includes the important role of surface step creation revises the above Rice criterion [33], but the effect is small for Ni. If  $K_{Ie} < K_{Ic}$ , the sharp crack is blunted by dislocation emission and this ultimately enables the failure by the ductile fracture mechanism of void nucleation, growth, and coalescence ahead of the crack [34]. If  $K_{Ic} < K_{Ie}$ , a sharp crack remains sharp and grows via cleavage with no dislocation emission; the energy dissipation in the plastic zone around the sharp crack is then much smaller than that for the ductile fracture mode.

In pure Ni, the (111) surface has the lowest surface energy,  $\gamma^s = 1.92 \text{ J/m}^2$  and hence  $\gamma^{\text{fr}} = 2\gamma^s = 3.84 \text{ J/m}^2$ , leading to  $K_{Ic} = 1.061 \text{ MPa}\sqrt{\text{m}}$ . For the most favorable crack orientation for emission from a (111) crack in Ni, the simulated and computed emission load in Ni at  $T=0 \text{ K}$  is in the range  $K_{Ie} = 0.73 - 0.77 \text{ MPa}\sqrt{\text{m}}$  depending on the interatomic potential and/or unstable stacking fault energy [27,35,36]. At finite temperature, thermally activated emission can take place at slightly lower loads with a small barrier. We thus consider emission to be in the range of  $K_{Ie} = 0.70 - 0.75 \text{ MPa}\sqrt{\text{m}}$ . The embrittlement condition is thus far from being met in hydrogen-free Ni. In terms of fracture energies, the embrittlement condition is  $\gamma^{\text{fr}} < \frac{\beta(\theta, \phi, \mathbf{C})}{\alpha(\mathbf{C})}\gamma_{\text{usf}} \approx 1.67 - 1.92 \text{ J/m}^2$  which, as seen in Fig. 1 ( $c_{\text{tip}} = 0$ ), is far from satisfied in pure Ni. Pure Ni is intrinsically ductile.

In the presence of H, embrittlement can be achieved if  $K_{Ie}$  is increased above  $K_{Ic}$  [13] or if  $K_{Ic}$  is decreased sufficiently to achieve

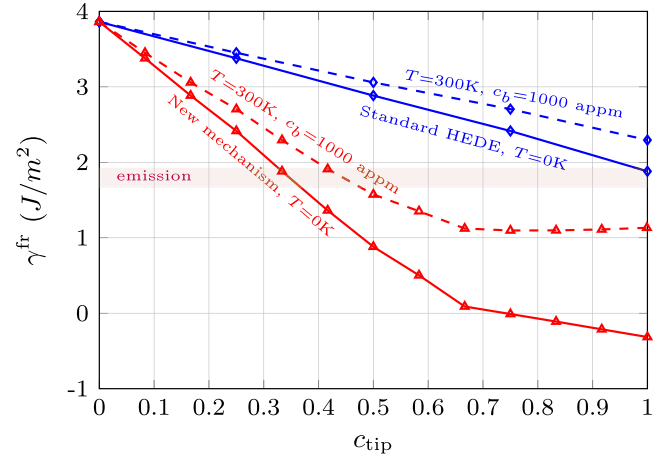


**Fig. 1.** Fracture energy (solid lines) and fracture free energy (dashed lines) versus crack tip H concentration  $c_{\text{tip}}$ , for the traditional HEDE model (blue) and the new mechanism involving aggregation and nanodiffusion at the crack tip (red). The range of fracture energies corresponding to the range of stress intensities for dislocation emission is indicated by the shaded region. Materials with fracture free energy above this region are ductile while materials with fracture free energy below this line are brittle. The energy at  $c_{\text{tip}} = 0$  corresponds to pure Ni, which is ductile. (For interpretation of the references to color in this figure legend, the reader is referred to the web version of this article.)

$K_{Ic} < K_{Ie}$ . In the new embrittlement scenario below,  $K_{Ic}$  is reduced well below  $K_{Ie} = 0.70 \text{ MPa}\sqrt{\text{m}}$ , or equivalently  $\gamma^{\text{fr}}$  is well below  $1.67 \text{ J/m}^2$  (see Fig. 1).

At finite temperatures and in the presence of H, embrittlement must consider the fracture and unstable stacking fault free energies. In the absence of H, these both decrease with increasing temperature by similar amounts [37,38]. Decreases in the elastic constants enter both processes equally. Thus, all of these finite-T effects are neglected here. What should not be neglected at finite T is the entropy change upon moving H from the (dilute) bulk to the (concentrated) fracture surface, and its contribution to the overall fracture free energy. We consider the general case where, after fracture, the H concentration on the newly formed Ni (111) surface is  $c_s$ . As discussed below, we also consider the H concentration in each of two subsurface layers to be  $c_{ss}$ . Specific cases will be considered in detail below. When the bulk H concentration in the sample is  $c_b$ , there is a change in entropy  $\Delta S$  in addition to the change in energy  $\Delta E$ . The fracture free energy per unit area then includes the entropic contribution  $T\Delta S/A_0$  where  $A_0 = 5.33\text{\AA}^2$  is the area per (111) surface site. Standard statistical mechanics analysis (see Appendix A) yields the fracture free energy as

$$\gamma^{\text{fr}} = \gamma_0^{\text{fr}} + \frac{2k_B T}{A_0} \{ (1 - c_s) \ln(1 - c_s) + c_s \ln c_s + (1 - c_{ss}) \ln(1 - c_{ss}) + c_{ss} \ln c_{ss} - (c_s + c_{ss}) \ln c_b \}$$

where  $\gamma_0^{\text{fr}}$  is the  $T=0$  fracture energy and  $k_B$  is Boltzmann's constant. In the remainder of this section, results involving the fracture free energy use a bulk H concentration  $c_b = 1000 \text{ appm}$ ; the entropic contribution to the fracture free energy over the range  $c_b = 300 - 3000 \text{ appm}$  typical of Ni embrittlement differs by only  $\pm 0.08 \text{ J/m}^2$ .

### 2.2. The HEDE model

The traditional HEDE model is shown in Fig. 2. H in the bulk Ni lattice diffuses to the crack tip, attracted by the pressure field around the tip (Fig. 2a). If H forms a single layer of H at concentration  $c_{\text{tip}} = 1.0$  of the octahedral sites just ahead of the crack (Fig. 2b) then after fracture there is an H surface coverage  $c_s = 0.5$  on each newly-created surface (Fig. 2c). The surface energy and

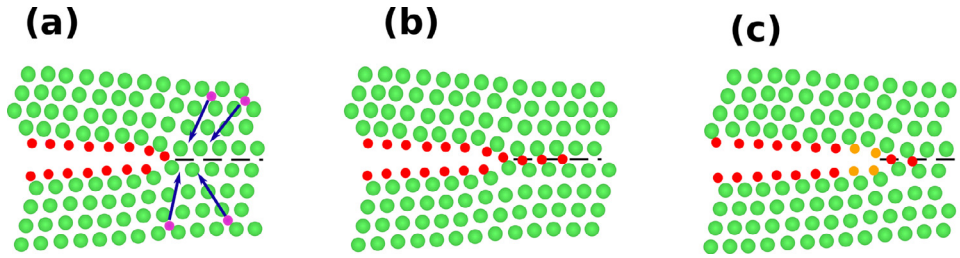


**Fig. 2.** Schematic of standard process of Hydrogen-enhanced decohesion. (a) Stress field of the crack attracts bulk H atoms to the crack tip; (b) H occupies a single layer of octahedral sites along the crack plane just ahead of the crack at concentration  $c_{\text{tip}}$  ( $c_{\text{tip}}=1.0$  shown for illustration); (c) the crack advances with the creation of two surfaces with H concentration  $c_s = c_{\text{tip}}/2$ ; the fracture energy for this process is too high even at  $c_{\text{tip}} = 1.0$  (see Fig. 1). Green: Ni atoms; Red and Orange: columns of Hydrogen atoms with 100% and 50% concentration, respectively. Dashed line indicates the cleavage plane. (For interpretation of the references to color in this figure legend, the reader is referred to the web version of this article.)

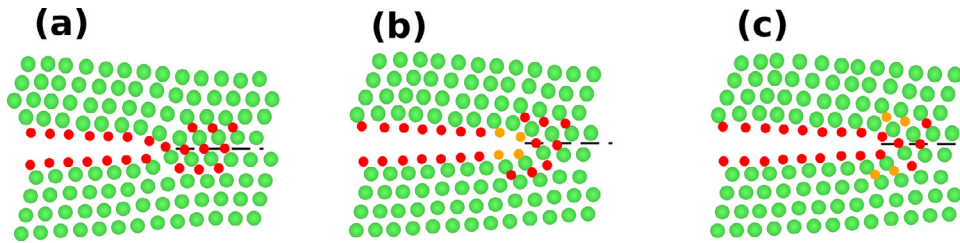


**Fig. 3.** Schematic of new hydrogen-induced decohesion process. (a) The crack tip stress field is sufficient to form a 3-layer hydrogen structure at the crack tip with concentration  $c_{\text{tip}}$  ( $c_{\text{tip}}=1.0$  shown for illustration); (b) the crack advances with new surfaces having surface concentration  $c_s = c_{\text{tip}}/2$  and subsurface concentrations  $c_{\text{ss}} = c_{\text{tip}}$ ; (c) Local nanoscale diffusion of the subsurface H to the surface increases  $c_{\text{ss}}$  up to  $c_{\text{ss}} = 1.0$ , reducing the fracture energy well below that necessary to cause the transition to cleavage fracture. Green: Ni atoms; Red and Orange: columns of Hydrogen atoms with 100% and 50% concentration, respectively. Dashed line indicates the cleavage plane. (For interpretation of the references to color in this figure legend, the reader is referred to the web version of this article.)

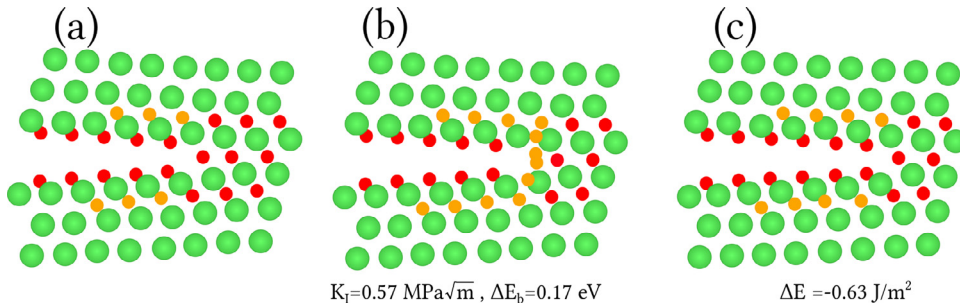


**Fig. 4.** Configurations during the fracture process as obtained by transition state Nudged Elastic Band simulations at  $K_I = 0.57 \text{ MPa}\sqrt{\text{m}}$ . (a) initial state, (b) transition state, (c) final state. The barrier for the overall process of propagation and nanodiffusion is 0.17 eV, with a substantial decrease in total energy at this load.

free energy up to  $c_s = 0.5$  ( $c_{\text{tip}} = 1.0$ ,  $c_{\text{ss}} = 0$ ) are shown in Fig. 1 as computed using DFT and a new Ni-H potential (see below); they are both above the embrittlement condition at both  $T=0 \text{ K}$  and, more importantly, at  $T=300 \text{ K}$ . Cleavage fracture thus cannot occur, quantifying the failure of the standard HEDE model for Ni.

### 2.3. New embrittlement mechanism

The new embrittlement mechanism is shown schematically in Figs. 3 and 4. It considers additional H diffusion to the crack tip sufficient to form at least a nanoscale 3-layer structure at high local H concentration  $c_{\text{tip}}$ ; Fig. 3 shows the limiting case of 100% occupation of the octahedral interstitial sites in each layer. When the 3-layer structure is fractured, two surfaces are again created, each with H surface coverage  $c_s = c_{\text{tip}}/2$  but now also with H occupation of  $c_{\text{ss}} = c_{\text{tip}}$  in each of the adjacent sub-surface layers (Fig. 3b). Most importantly, H in each sub-surface layer can diffuse to the new crack surface via a single atomic hop, increasing the surface coverage up to  $c_s = c_{\text{tip}}/2 + c_{\text{tip}} = 3c_{\text{tip}}/2$  up to  $c_s = 1.0$  (saturation) of both fracture surfaces, with remaining H in the sub-surfaces.

The processes of cleavage and single-atomic-hop motion to reduce the fracture energy to zero, as shown occurring in Fig. 4 by a two-step sequence, can actually occur simultaneously in a single thermally-activated step. This is demonstrated by Nudged Elastic Band simulations of the transition path and associated energy barrier between the initial state shown in Fig. 4a, the transition state shown in Fig. 4b, and the final state shown in Fig. 4c, computed at  $K_I = 0.57 \text{ MPa}\sqrt{\text{m}} < K_{Ic}$ . For illustration, we use a periodic crack front length of  $4.96 \text{ \AA}$ , the limiting case  $c_{\text{tip}} = 1.0$ , and we use our new modified Ni-H EAM potential (see Appendix C). At this load, the barrier for the full process including the subsurface nanodiffusion is  $\approx 0.17 \text{ eV}$  and the final state is much lower in energy ( $-0.63 \text{ J/m}^2$  when converted to an effective surface energy) than the initial state due to the saturation of H on the final crack surfaces. The cleavage process is thus energetically favorable at a load well below the emission load. The barrier of 0.17 eV is close to the DFT-computed barrier for H to migrate from the sub-surface to the surface, and is very low so that the entire process is fast at room temperature. NEB simulations at an even lower  $K_I = 0.40 \text{ MPa}\sqrt{\text{m}}$  have a similar barrier but a very small energy difference of  $-0.06 \text{ J/m}^2$ ,



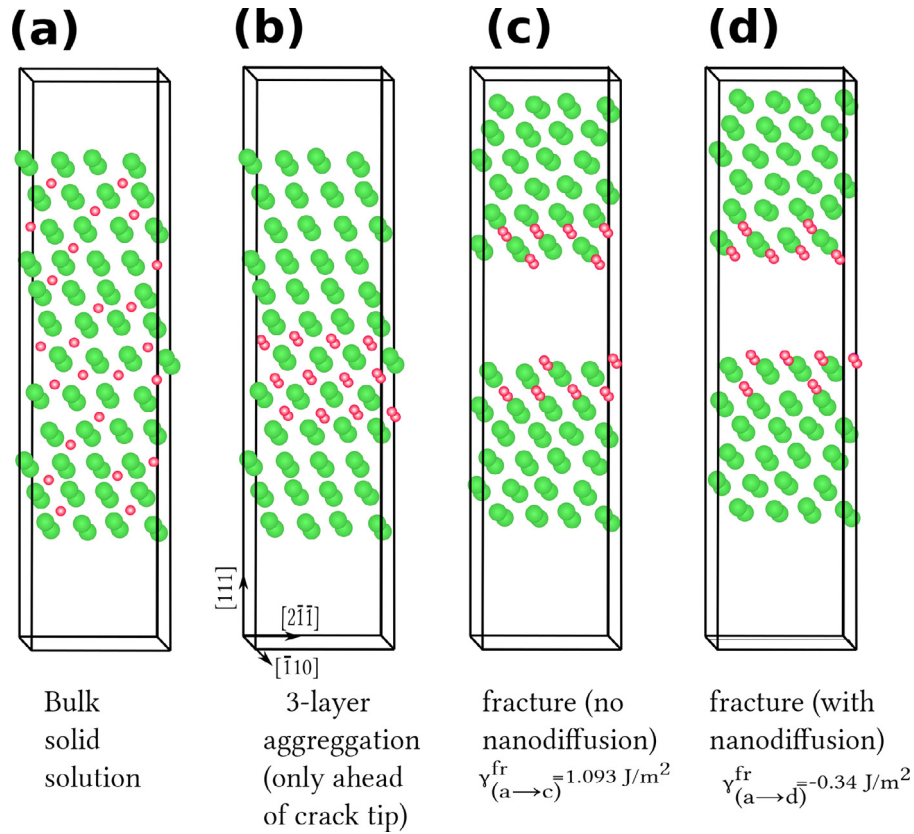


**Fig. 5.** H configurations relevant to the new fracture mechanism, and corresponding DFT computations of their energy. (a) Solid solution schematic (actual computation performed for a single H in a bulk Ni structure); this is the reference energy; (b) the 3-layer hydride that forms ahead of the crack tip (for  $c_{\text{tip}} = 1.0$ ) - this structure does not form in the bulk material **due to entropy**; (c) intermediate state of the fractured 3-layer hydride with no diffusion of sub-surface H; (d) final fractured 3-layer hydride after local diffusion from the subsurface to the free surfaces. The associated fracture energies and cleavage stress intensities are indicated under subfigures c and d. Green and red spheres denote Ni and H atoms, respectively. (For interpretation of the references to color in this figure legend, the reader is referred to the web version of this article.)

indicating that  $K_I = 0.40 \text{ MPa}\sqrt{m}$  is near the minimum load for the overall cleavage process to be energetically favorable at  $c_{\text{tip}} = 1.0$ .

The energies for the **relevant configurations** involved in the new mechanism are computed using first-principles DFT as shown in Fig. 5 for  $c_{\text{tip}} = 1.0$ . **Aggregation of H into the three layer structure is energetically favorable (Fig. 5b) in the bulk but is not entropically favorable in the bulk, and so only occurs at the crack tip, as discussed in Section 3.** The intermediate fractured state with subsurface H (Fig. 5c), although not crucial to the analysis, has a lower fracture energy than in the absence of the subsurface H. The final fracture energy after nanodiffusion (Fig. 5d) is **negative** for  $c_{\text{tip}} = 1.0$ .

The fracture energy and fracture free energy in the final state where nanodiffusion has occurred during the fracture process (see Fig. 3c) are shown versus the crack tip concentration  $c_{\text{tip}}$  in Fig. 1. Calculations using DFT and using the new Ni-H potential are essentially identical (see Appendix C). For the **free energy calculation**, the amount of H diffusing from the subsurfaces to the surface is the value that minimizes the fracture free energy. Denoting the concentration of H that undergoes nanodiffusion as  $c_{\text{ss-s}}$ , the concentrations after fracture are  $c_s = c_{\text{tip}} + 2c_{\text{ss-s}}$  and  $c_{\text{ss}} = c_{\text{tip}} - c_{\text{ss-s}}$ . The **entropic contribution** increases the fracture free energy above the  $T=0$  K fracture energy but the strong reduction in surface energy at near-100% surface occupation of H still leads to a fracture free energy that is below the embrittlement condition for  $c_{\text{tip}} > 0.5$ . This embrittlement condition is only slightly above the minimum value  $c_{\text{tip}} \approx 0.375$  predicted at  $T=0$  K.

Atomistic simulations at  $T=0$  K without the nanodiffusion process further validate the above embrittlement mechanism. For

$c_{\text{tip}} = 1.0$  in the single layer of H ahead of the crack tip (Fig. 2b), the crack emits dislocations and thus blunts at  $K_I = 0.73 \text{ MPa}\sqrt{m}$ , as predicted by the theory. The presence of the H has essentially no effect; this again shows the failure of the HEDE model. For  $c_{\text{tip}} = 1.0$  in the 3-layer structure ahead of the crack tip (Fig. 3a), the crack cleaves at  $K_I = 0.656 \text{ MPa}\sqrt{m}$ . The  $T=0$  K cleavage load (without nanodiffusion) is predicted to be  $K_I = 0.57 \text{ MPa}\sqrt{m}$  ( $\gamma_0^{\text{fr}} = 1.093 \text{ J/m}^2$ , see Fig. 5c) for this configuration. The difference is due, in part, to the release of the mechanical energy of the H interstitials ahead of the crack, which plays a role similar to the entropic loss because aggregation at the crack tip is achieved at the cost of the solid solution entropy (see below).

Finally, we note that full equilibrium between H in the bulk solid solution and H on the free (111) Ni surface is achieved when the chemical potentials are equal. Because the binding energy of H to the (111) surface is strong,  $\Delta E_s = -0.54 \text{ eV}$  relative to H in solid solution, the equilibrium surface concentration  $c_s = c_b \exp(-\Delta E_s/k_B T)/(1 + c_b \exp(-\Delta E_s/k_B T))$  is essentially  $c_s = 1.0$  at  $T=300$  K and all relevant values of the bulk concentration. Thus, after fracture to create new surface, further H will diffuse to any newly formed but unoccupied surface sites to achieve the equilibrium concentration  $c_s = 1.0$ .

**Based on the above analysis, we can conclude that the overall process of H embrittlement in Ni occurs by formation of (at least) a 3-layer nanostructure just ahead of the crack tip followed by fracture during which nanodiffusion from the subsurface brings sufficient H to the surface to reduce the fracture free energy below the level needed for embrittlement. This is the main result of this paper.**

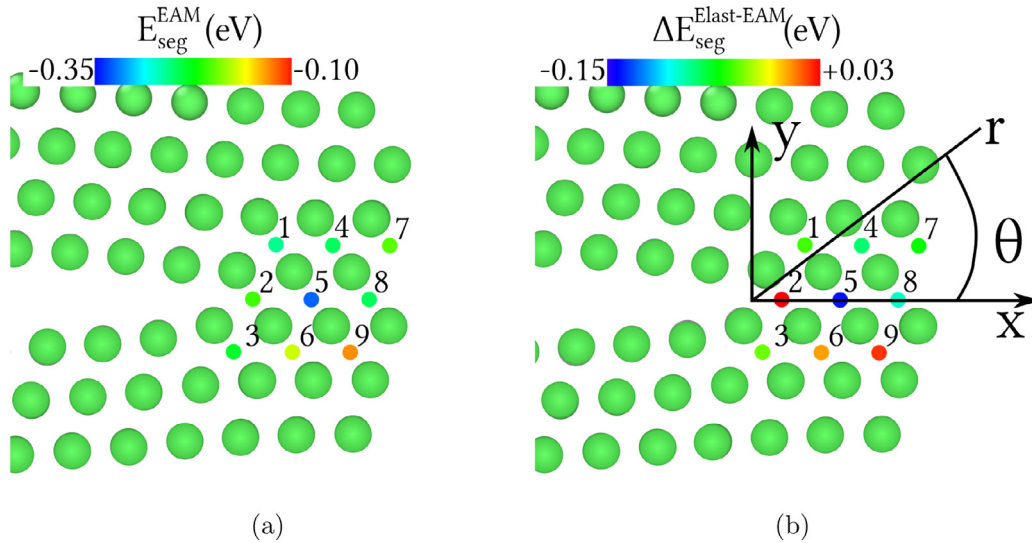


**Fig. 6.** (a) Segregation energies for H at sites in the 3-layer region around the crack tip as calculated by atomistic simulations and (b) the difference  $\Delta E_{\text{seg}}^{\text{Elast-EAM}}$  in H segregation energies using the elasticity and atomistic simulation. The local crack tip coordinates are also shown in (b).

### 3. Thermodynamics and kinetics considerations

#### 3.1. H aggregation at the crack tip

For the new cleavage process to occur, the aggregation of H to form the 3-layer structure at concentration  $c_{\text{tip}}$  ahead of the crack tip must be thermodynamically possible at the applied stress intensities below  $K_{\text{Ie}}$  that are required for embrittlement. Aggregation is computed using an equilibrium thermodynamic simple-solution model. In equilibrium, the chemical potential of H is constant throughout the material. Far from the crack, the chemical potential  $\mu_{\text{H}}$ , relative to the dilute heat of solution of H in Ni, is solely entropic. At position  $\mathbf{x} = (r, \theta)$  near the crack, the  $\mu_{\text{H}}$  has a contribution  $p(r, \theta)\Delta V$  due to the interaction of the hydrostatic stress field  $p$  around the crack with the misfit volume  $\Delta V$  of interstitial H. There is also a contribution due to attractive H-H interactions  $E_{\text{HH}}$  [39]. Equating  $\mu_{\text{H}}$  in the far-field and at the crack, the H concentration  $c(r, \theta)$  is related to the far-field bulk H concentration  $c_{\text{b}}$  as

$$\begin{aligned} \mu_{\text{H}} &= k_{\text{B}}T \log \left( \frac{c_{\text{b}}}{1 - c_{\text{b}}} \right) \\ &= k_{\text{B}}T \log \left( \frac{c(r, \theta)}{1 - c(r, \theta)} \right) - p(r, \theta)\Delta V + c(r, \theta)E_{\text{HH}} \end{aligned} \quad (1)$$

The hydrostatic stress field around the crack provides the major driving force for the aggregation of H at the crack tip. The pressure field around the crack can be estimated using isotropic elasticity as

$$p(r, \theta) = \frac{2(1 + \nu)K_{\text{I}}}{3\sqrt{2\pi}r} \cos \frac{\theta}{2} \quad (2)$$

where  $\nu$  is Poisson's ratio. The applicability of elasticity for determining the contribution  $p(r, \theta)\Delta V$  to  $\mu_{\text{H}}$  is verified by direct calculation of the energies of single H atoms at various octahedral sites (indicated in Fig. 3a) around the crack tip. The segregation energies predicted by atomistic simulations using the new Ni-H EAM potential,  $E_{\text{seg}}^{\text{EAM}}$ , and differences between the elastic and atomistic predictions,  $\Delta E_{\text{seg}}^{\text{Elast-EAM}} = E_{\text{seg}}^{\text{EAM}} - E_{\text{seg}}^{\text{elas}}$ , for each site in the three layered hydride are shown in Figs. 6a and b at  $K_{\text{I}} = 0.57 \text{ MPa}\sqrt{\text{m}}$ , respectively. The numerical values are given in Table D1. Differences between atomistics and elasticity are small and negative, so the

elastic prediction is accurate and conservative. Even better agreement is achieved at lower  $K_{\text{I}}$  values.

The hydride region necessary for crack propagation encompasses sites # 1–6 (see Fig. 6a). Site # 4 has the lowest binding of H atoms and so dictates the value of  $p\Delta V$  used in Eq. (2). Specifically, the position  $(r, \theta)$  of site # 4 is inserted into Eq. (2). The predicted H concentration  $c_{\text{tip}}$  at the crack tip as a function of temperature  $T$ , bulk H concentration  $c_{\text{b}}$ , and applied  $K_{\text{I}}$  is shown in Fig. 7(a).

Reaching the embrittlement concentration of  $c_{\text{tip}} \approx 0.5$  over the 3 at. layers at the crack tip is achievable for  $c_{\text{b}} > 300 \text{ appm}$  at  $K_{\text{I}} = 0.57 \text{ MPa}\sqrt{\text{m}}$  at  $T = 300 \text{ K}$ . Thus, the necessary conditions can be achieved for H concentrations at which embrittlement is observed in Ni. At  $K_{\text{I}} = 0.40 \text{ MPa}\sqrt{\text{m}}$  a bulk concentration of  $c_{\text{b}} = 2000 \text{ appm}$  would be required to achieve  $c_{\text{tip}} = 0.5$  at the crack tip. The NEB simulations in the preceding section show that fracture is feasible at this lower  $K_{\text{I}}$  for  $c_{\text{tip}} = 1.0$ . H embrittlement in Ni at room temperature thus requires a concentration between 300–1000 appm, consistent with the range observed experimentally.

Fig. 7 (a) suggests that embrittlement is more feasible at low  $T$  because H aggregation is strongly enhanced. However, the aggregation requires H diffusion to the crack tip and the diffusion rate decreases rapidly as the temperature decreases. Diffusion to the crack tip is controlled by the diffusion far from the crack to the near-crack region. There are no anomalous barriers to transport in and around the crack tip, as verified by both NEB and direct MD simulations of H barriers and motions near the crack tip with and without aggregated H. The kinetics of H transport to the crack tip was considered by Song et al. [28] for a specified crack tip loading rate  $\dot{K}_{\text{I}}$ . The number of H atoms per unit crack length  $N/L_{\text{z}}$  was derived as

$$N/L_{\text{z}} = A_0 K_{\text{I}}^{\frac{8}{5}}; A_0 = \beta \left( \frac{1}{2}, \frac{9}{10} \right) \frac{4c_{\text{b}}}{a_0^3} \left( \frac{5(1 + \nu)D\Delta V}{12\sqrt{2\pi}k_{\text{B}}T\dot{K}_{\text{I}}} \right)^{\frac{4}{5}} \quad (3)$$

with lattice parameter  $a_0 = 3.52 \text{ \AA}$ , diffusion coefficient  $D = D_0 \exp(-E_{\text{b}}/k_{\text{B}}T)$ , and  $\beta(\frac{1}{2}, \frac{9}{10})$  the  $\beta$ -function. Considering the initial cracks that cause embrittlement to have a length equal to the typical grain size  $d$  in a polycrystalline sample, Song and Curtin [27] estimated the typical loading rate  $\dot{K}_{\text{I}}$  associated with a tension test at strain rate  $\dot{\epsilon}$  as  $\dot{K}_{\text{I}} = E\dot{\epsilon}\sqrt{2\pi}d$  where  $E$  is the Young's modulus. For polycrystalline Ni with grain sizes  $d = 10 - 100 \mu\text{m}$

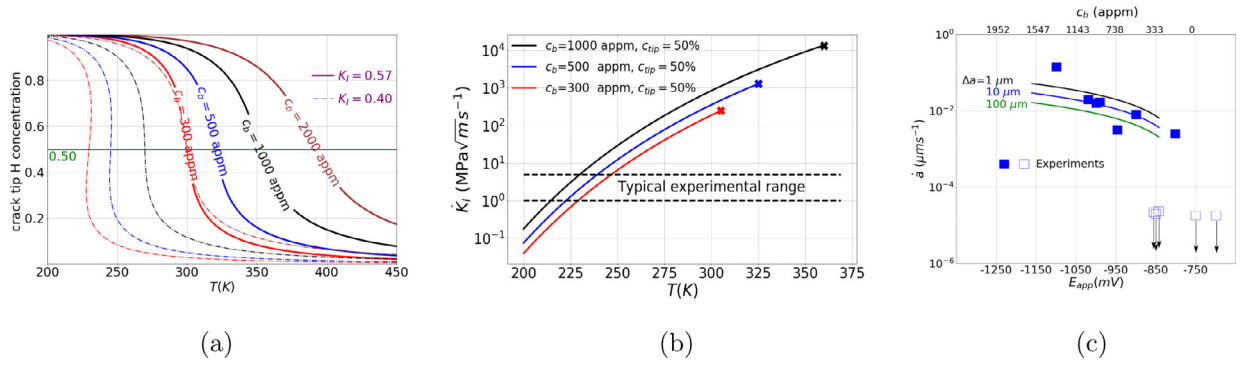


**Fig. 7.** (a) Crack tip H concentration  $c_{tip}$  versus temperature for various bulk H concentrations  $c_b$  and applied stress intensities  $K_I$ . The green line indicates the minimum crack tip concentration  $c_{tip} \approx 0.5$  needed for embrittlement (see Fig. 1); (b) Maximum K-loading rate required for formation of the 3-layer hydride for various  $c_b$  and applied  $K_I$ , with lines terminating at the thermodynamic limit for embrittlement; (c) Computed and measured crack growth rates versus applied electrical potential field. Lines: predictions rate for measurements made over varying amounts of crack growth in the experimental range; Symbols: experimental data on Monel-500 Ni alloy [40] with open symbols indicating no crack growth at the limit of experimental resolution. (For interpretation of the references to color in this figure legend, the reader is referred to the web version of this article.)

and standard uniaxial loading rate  $\dot{\epsilon} = 10^{-4}\text{s}^{-1}$ , the estimated crack tip loading rates are in the range  $1 - 3 \text{ MPa}\sqrt{\text{m}}\text{s}^{-1}$  [27].

For Ni,  $D_0 = 1.8611 \times 10^{-6}\text{m}^2/\text{s}$  and  $E_b = 0.46\text{eV}$ . Formation of the 3-layer hydride over a distance of two lattice constants corresponds to  $N/L_z = 6.04\text{H}/\text{nm}^{-1}$  for  $c_{tip} = 0.50$ . This value and the embrittling concentrations  $c_b$  dictate the maximum loading rate below which H aggregation can be achieved prior to reaching the dislocation emission threshold. At  $K_I = 0.57 \text{ MPa}\sqrt{\text{m}}$  and  $c_b = 1000$  appm, the loading rate must be  $\dot{K}_I \approx 850 \text{ MPa}\sqrt{\text{m}}\text{s}^{-1}$  for  $c_{tip} = 0.5$ . This upper limit is reduced to  $\approx 200 \text{ MPa}\sqrt{\text{m}}\text{s}^{-1}$  for  $c_b = 300$  appm. These maximum K-loading rates are far larger than experimental rates. Fig. 7b shows the maximum allowed loading rate vs. temperature for Ni, for various concentrations and  $K_I$  values. Embrittlement at  $T=200$  K requires very slow loading rates,  $\dot{K}_I < 0.1 \text{ MPa}\sqrt{\text{m}}\text{s}^{-1}$ , below those typically used. The kinetics of aggregation of H at the crack tip is thus consistent with embrittlement at  $T=300$  K,  $c_b \approx 300 - 1000$  appm, and strain rates  $\approx \dot{\epsilon} = 10^{-4}\text{s}^{-1}$ , as seen experimentally. Embrittlement at  $T=200$  K or lower is not predicted to be achievable at typical loading rates. We discuss recent measurement of some embrittlement in Ni at 77 K in the Discussion [22].

### 3.2. Slow crack growth

Once the initial 3-layer structure has formed and embrittlement can commence, further crack growth occurs at a rate dictated by the diffusion of additional H to the crack tip region. Only enough H to cover the new surfaces is required. As for the aggregation, this diffusion is controlled by the long-range diffusion to the crack tip region. The average crack growth rate due to this diffusion was derived by Song et al. [28] as

$$\dot{a} = \frac{da}{dt} = \frac{4}{\pi} \frac{D\Delta V}{k_B T} \frac{(1+\nu)K_I}{3\sqrt{2\pi}} \left(\frac{\pi c_b}{a_0}\right)^{3/2} \Delta a^{-1/4} \quad (4)$$

where  $\Delta a$  is the increase in the length of the crack. Crack growth is typically measured after some amount of crack growth but depends weakly on the amount of crack growth. Using the H diffusion rate and at the critical cleavage load, the crack growth rate after crack growth of  $\Delta a$  can be computed.

Crack growth experiments on the Ni-based alloy Monel K-500 were carried out by [40] using electrochemical methods at room temperature. They determined a relationship between the diffusible H concentration  $c_b$  and the electric potential  $V$  in millivolts as  $V = -0.2471(c_b(\text{appm}) + 3106)$  and measured the crack growth rate as a function of  $V$ . The onset of embrittlement was found to occur in the range of  $V = -850$  mV to  $V = -750$  mV. We consider

embrittlement at the minimum predicted concentration 300 appm (see Fig. 7(a)) and consider values of  $\Delta a$  in the range used in the experiments. Fig. 7c shows the predicted crack growth rate versus electric potential  $V$  in millivolts using the V-H relationship of [40]. Good overall agreement is achieved in both magnitude and trend, with no adjustable parameters.

### 4. Cleavage along grain boundaries

The one important remaining issue is the role of the grain boundaries in the embrittlement process. Experimental observations show that H embrittlement in Ni is associated with intergranular fracture. Our analysis above is based on H at the crack tip in bulk Ni. At grain boundaries, there is equilibrium segregation even in the absence of a crack. So, additional aggregation due to the crack tip fields and subsurface H might not be necessary for embrittlement. We revisit the analysis of Tehranchi and Curtin [41] using the new more-accurate Ni-H potential. This potential is still imperfect for grain boundary energies (see Appendix E) but appears sufficient.

We consider four fracture energies associated with different states of H aggregation around a range of symmetric tilt boundaries in Ni. The first case is the fracture energy in the absence of H. The second case is the fracture energy for equilibrium segregation of H to the GB at  $T=0$  K; this corresponds to occupying all H binding sites in the GB with H, and so is the maximum possible amount of segregation in the absence of crack tip fields. The third case follows from the second case by considering local diffusion of all H that is not on the final GB fracture surfaces to the GB fracture surfaces, where we select the lowest fracture energy surface among possible fracture paths [41]. The fourth case corresponds to 100% coverage of both fractured GB surfaces. The fourth case thus requires both additional aggregation of H around a crack tip and the subsequent local diffusion of that H to the final fracture surface. This fourth case is the situation that we have shown drives embrittlement in bulk Ni.

Fig. 8 shows the critical stress intensities for cleavage associated with each of above four scenarios, across a range of grain boundaries in Ni. The critical stress intensity for dislocation emission for a crack along each grain boundary is also shown. Embrittlement is again predicted if  $K_{Ic} < K_{Ie}$ . The analysis predicts that embrittlement is not possible in any of the first three scenarios that do not include additional H aggregation due to the presence of a crack tip. The only exception is the case nanodiffusion in  $\Sigma 19(331)$  in which  $K_{Ic}$  is slightly lower than  $K_{Ie}$ . Only when additional H is added to

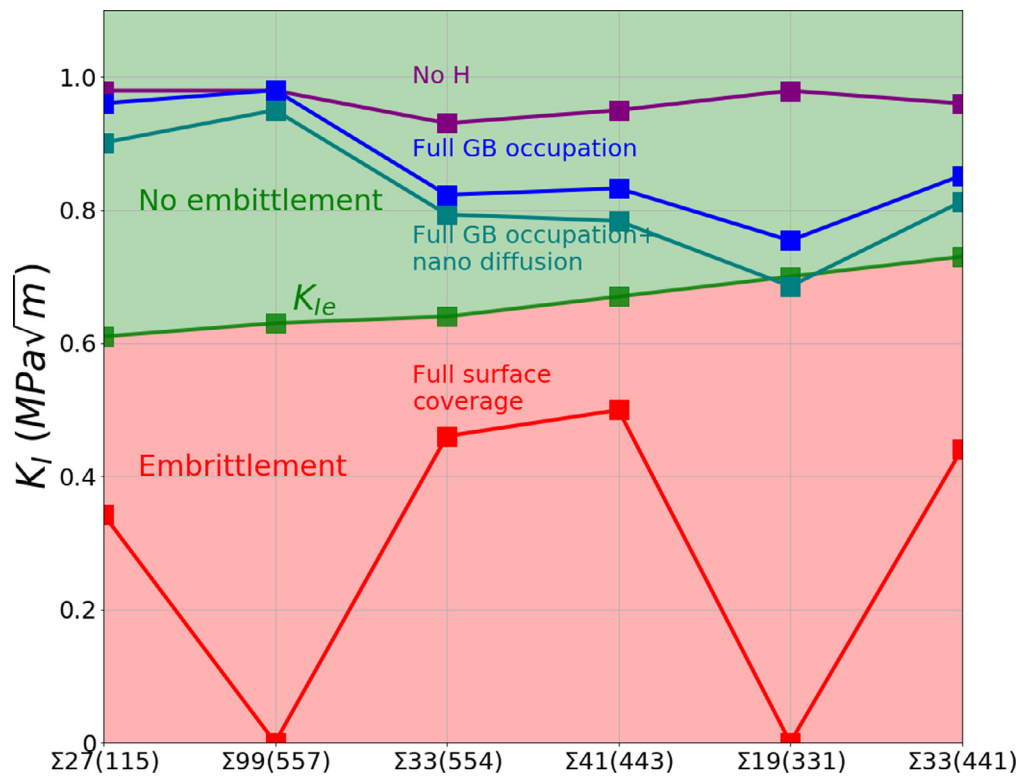


**Fig. 8.** Critical stress intensities for cleavage and emission of dislocation for different grain boundaries in nickel. The purple, blue, bluegreen, and red lines indicate the  $K_{Ic}$  for the cases with no H along the GB, all GB sites filled with H atoms, all GB sites filled H atoms and nanodiffusion brings them to surface, and all surface sites filled with H, respectively. The green line denotes  $K_{Ic}$ . The green and red regions are the ductile and brittle domains, respectively. (For interpretation of the references to color in this figure legend, the reader is referred to the web version of this article.)

saturate the fracture surfaces of each GB do we find that there is a precipitous drop in  $K_{Ic}$  and a transition to brittle behavior.

The above is not a complete mechanics, thermodynamics, and kinetics analysis of the processes that will embrittle grain boundaries. Such studies can follow in the future, and are particular to each grain boundary. The important feature is that the same mechanism is necessary for embrittlement. The second important feature is that since the  $K_{Ic}$  values are larger for these GBs as compared to crystalline Ni, and since some H is already present due to equilibrium segregation (not shown), embrittlement along grain boundaries is generally easier to achieve. This is consistent with the experimental observation of intergranular cleavage fracture along grain boundaries.

## 5. Discussion

The present work is complementary to the nano-hydride formation mechanism proposed by Song and Curtin [27,28]. In that theory, the nanohydride blocks the emission of the dislocations (i.e. increases the  $K_{Ic}$  to much higher values), so that cleavage then becomes possible. Here, in Ni, the presence of only a 3-layered nano-hydride with concentration as low as  $c_{tip} = 0.5$  ahead of the crack can instead reduce  $K_{Ic}$  below  $K_{Ic}$ , leading to cleavage. The mechanism presented here may not operate in other materials, and then the mechanism of Song and Curtin would become relevant.

The analysis here can also be considered in some respects as a version of the “defactant” theory within the HEDE framework. The “defactant” theory would state that because the surface energy of the 100% H-saturated Ni surface can be nearly zero, or very low along some grain boundaries, that embrittlement must occur. “Defactant” theory does not, however, address the physical pathway for achieving this final state. Since H embrittlement is known to be time-dependent, kinetics is essential. The present work demon-

strates the physical and kinetic pathway for achieving the final state.

We have neglected quantum effects. However, Di Stefano et al. [42] showed that zero-point energies and quantum tunnelling do not play a crucial role in the diffusion of H in Nickel. Such effects on the energetics of H are also neglected; since all comparisons here are differences between bulk and surface H energies, the quantum effects may be small.

Recent experiments on polycrystalline Ni show some embrittlement features at  $c_b \approx 4500$  appm at  $T=77$ K [22] after segregation at  $T=293$ K, suggesting that diffusion is not necessary for embrittlement. The observed embrittlement features are some grain boundary microcracks interspersed on the ductile fracture surface, and a small “reduction in area” at final fracture. However, unlike the same material at  $T=293$ K, the specimen has nearly the same failure strain and ultimate tensile strength, and shows the onset of necking prior to final failure. Thus, there is evidence of some embrittlement at  $T=77$ K but it is far less severe than at  $T=293$  K. These findings are rationalized by two aspects. First, there may be some GBs that can be embrittled purely by segregation at  $T=293$  K; studies to date are only on a few symmetric tilt boundaries. These rare GBs would generally be insufficient in number to drive significant macroscopic embrittlement but would appear as cracked. Second, and more importantly, forthcoming first-principles work [43] shows that, among 20 GBs studied, several symmetric tilt GBs have continuous low-barrier H diffusion paths along or perpendicular to the tilt axis ( $\Sigma 9(100)(221)$ : 0.16 eV;  $\Sigma 11(110)(332)$ : 0.12 eV;  $\Sigma 5(100)(310)$ : 0.2 eV;  $\Sigma 17(100)(140)$ : 0.23 eV). It can be anticipated that there are many other GBs with such low diffusion barriers that are sufficient for H transport even at  $T=77$ K. However, since these would be only a small fraction of all GBs, embrittlement would be localized and limited. This is again consistent with the observations at  $T=77$  K.



The present model should apply to other fcc systems, such as fcc Fe and related stainless steels, and new fcc High Entropy Alloys. The CoCrFeMnNi Cantor Alloy has recently been shown to be more resistant to H embrittlement than standard austenitic stainless steels [44–46] but still embrittles at very low loading rates [47]. Our analysis can be extended to these more-complex systems and rationalizes these new experimental findings. We will report on such analyses in the near future.

In summary, we have developed a full model for the embrittlement of Ni by H encompassing the mechanical, thermodynamic, and kinetic conditions needed to achieve embrittlement. The essential new feature of the theory is the role of multilayer aggregation at the crack tip, leading to the diffusion of subsurface H, via only one atomic hop, to reduce the surface energy to nearly zero and the surface free energy sufficiently for embrittlement. We predict embrittlement via the onset of cleavage at  $c_b = 300 - 1000$  appm at room temperature, limited embrittlement at temperatures  $T < 200$  K, slow crack growth behavior consistent with experimental rates, and with an preliminary energetic analysis of the same mechanism for embrittlement along grain boundaries. All of these features are quantitatively or qualitatively in agreement with experiments on embrittlement in fcc Ni.

### Declaration of interests

The authors declare that they have no known competing financial interests or personal relationships that could have appeared to influence the work reported in this paper.

### Acknowledgment

WAC and AT gratefully acknowledge prior support of this work from the [Swiss National Science Foundation](#) through a grant for the project entitled “Predictive Mechanisms of Hydrogen Embrittlement” (project # 200021-149207).

### Appendix A. Free energy of fracture

Consider a body of  $N_{\text{Ni}}$  nickel atoms without any surface.  $N_H^0$  hydrogen atoms reside in the octahedral sites in the bulk crystal. The multiplicity of states is

$$\omega_1 = \frac{S_B^0!}{(S_B^0 - N_H^0)!N_H^0!} \quad (\text{A.1})$$

where  $S_B^0$  is number of the octahedral sites in the bulk. After fracture, two surfaces and two subsurfaces are formed. Some number  $N_H^s$  atoms move from the bulk to reside on the surface. In addition,  $N_H^{ss}$  move from the bulk and reside in the two subsurfaces.  $N_H^B$  atoms remain in the bulk material, with  $N_H^0 = N_H^s + N_H^B + N_H^{ss}$ . Now the multiplicity of states for this configuration of H atoms is then

$$\omega_2 = \frac{S_B!}{(S_B - N_H^B)!N_H^B!} \times \frac{S_s!}{(S_s - N_H^s)!N_H^s!} \times \frac{S_{ss}!}{(S_{ss} - N_H^{ss})!N_H^{ss}!} \quad (\text{A.2})$$

where  $S_s$  and  $S_{ss}$  are the numbers of surface and subsurface sites, respectively.  $S_B = S_B^0 - \frac{1}{2}S_s - S_{ss}$  is the number of bulk sites in the fractured body since the octahedral sites on the fracture plane and its adjacent subsurface planes have become surface and subsurface sites. The number of octahedral sites on the two dimensional fracture planes in comparison with the number of octahedral sites in the three dimensional bulk is negligible, and so we can approximate  $S_B^0 \approx S_B$ .

The number of surface sites for one surface is equal to  $A/A_0$  where  $A$  is the surface area and  $A_0 = 5.33\text{\AA}^2$  is the area per octahedral site on a (111) plane. Thus, the number of surface sites of

the fractured body  $S_s = 2A/A_0$ . The number of the subsurface octahedral sites of the fcc (111) plane is the same as the number of surface sites. Thus the number of subsurface sites of the fractured body is also  $S_{ss} = S_s = 2A/A_0$  but we keep  $S_{ss}$  and  $S_s$  different until the end of the derivation.

The change in the entropy of the system upon fracture is then

$$\Delta S = -k_B (\ln \omega_2 - \ln \omega_1). \quad (\text{A.3})$$

Using Stirling's approximation  $\ln n! \approx n \ln n - n$  throughout, we have

$$\begin{aligned} \ln \omega_1 &= S_B \ln S_B - S_B - ((S_B - N_H^0) \ln (S_B - N_H^0) - (S_B - N_H^0)) \\ &\quad - (N_H^0 \ln N_H^0 - N_H^0) \\ &= S_B \ln \frac{S_B}{S_B - N_H^B - N_H^s - N_H^{ss}} + (N_H^B + N_H^s + N_H^{ss}) \\ &\quad \ln \frac{(S_B - N_H^B - N_H^s - N_H^{ss})}{N_H^B + N_H^s + N_H^{ss}} \end{aligned} \quad (\text{A.4})$$

$$\begin{aligned} \ln \omega_2 &= S_s \ln S_s - S_s - ((S_s - N_H^s) \ln (S_s - N_H^s) - (S_s - N_H^s)) \\ &\quad - (N_H^s \ln N_H^s - N_H^s) + S_{ss} \ln S_{ss} - S_{ss} - ((S_{ss} - N_H^{ss}) \\ &\quad \ln (S_{ss} - N_H^{ss}) - (S_{ss} - N_H^{ss})) - (N_H^{ss} \ln N_H^{ss} - N_H^{ss}) \\ &\quad + S_B \ln S_B - S_B - ((S_B - N_H^B) \ln (S_B - N_H^B) - (S_B - N_H^B)) \\ &\quad - (N_H^B \ln N_H^B - N_H^B) \\ &= S_B \ln \frac{S_B}{S_B - N_H^B} + N_H^B \ln \frac{(S_B - N_H^B)}{N_H^B} + S_s \ln \frac{S_s}{S_s - N_H^s} \\ &\quad + N_H^s \ln \frac{(S_s - N_H^s)}{N_H^s} + S_{ss} \ln \frac{S_{ss}}{S_{ss} - N_H^{ss}} + N_H^{ss} \ln \frac{(S_{ss} - N_H^{ss})}{N_H^{ss}} \end{aligned} \quad (\text{A.5})$$

The change in the entropy is then

$$\begin{aligned} \frac{\Delta S}{-k_B} &= \ln \omega_2 - \ln \omega_1 \\ &= S_B \ln \frac{1 - c_b - N_H^s/S_B - N_H^{ss}/S_B}{1 - c_b} \\ &\quad + N_H^B \ln \frac{(1 - c_b)}{c_b} \frac{c_b + N_H^s/S_B + N_H^{ss}/S_B}{(1 - c_b - N_H^s/S_B - N_H^{ss}/S_B)} \\ &\quad + N_H^s \ln \frac{(1 - c_s)}{c_s} \frac{c_b + N_H^s/S_B + N_H^{ss}/S_B}{(1 - c_b - N_H^s/S_B - N_H^{ss}/S_B)} + S_s \ln \frac{1}{1 - c_s} \\ &\quad + N_H^{ss} \ln \frac{(1 - c_{ss})}{c_{ss}} \frac{c_b + N_H^s/S_B + N_H^{ss}/S_B}{(1 - c_b - N_H^s/S_B - N_H^{ss}/S_B)} + S_{ss} \ln \frac{1}{1 - c_{ss}} \end{aligned} \quad (\text{A.6})$$

Here  $c_s = N_H^s/S_s$  and  $c_{ss} = N_H^{ss}/S_{ss}$  are the concentration of the H atoms on the fracture two surfaces and two subsurfaces. Since the number of H atoms at the surface,  $N_H^s$ , and subsurface  $N_H^{ss}$ , are far less than the number of the octahedral sites in the bulk,  $N_H^s/S_B \approx 0$  and  $N_H^{ss}/S_B \approx 0$ . Thus, we arrive at

$$\begin{aligned} \frac{\Delta S}{-k_B} &= S_B \ln \underbrace{\frac{1 - c_b}{1 - c_b}}_{=0} + N_H^B \ln \underbrace{\frac{(1 - c_b)}{c_b} \frac{c_b}{(1 - c_b)}}_{=0} \\ &\quad + N_H^s \ln \frac{(1 - c_s)}{c_s} \frac{c_b}{(1 - c_b)} + S_s \ln \frac{1}{1 - c_s} \\ &\quad + N_H^{ss} \ln \frac{(1 - c_{ss})}{c_{ss}} \frac{c_b}{(1 - c_b)} + S_{ss} \ln \frac{1}{1 - c_{ss}} \end{aligned} \quad (\text{A.7})$$

In the fcc (111) plane the number of the surface and subsurface octahedral sites are the same,  $S_{ss} = S_s = n_s$ , and so

$$\begin{aligned} \frac{\Delta S}{-k_B n_s} &= -(1 - c_s) \ln(1 - c_s) - c_s \ln c_s + c_s \ln c_b \\ &\quad - (1 - c_{ss}) \ln(1 - c_{ss}) - c_{ss} \ln c_{ss} + c_{ss} \ln c_b \end{aligned} \quad (\text{A.8})$$



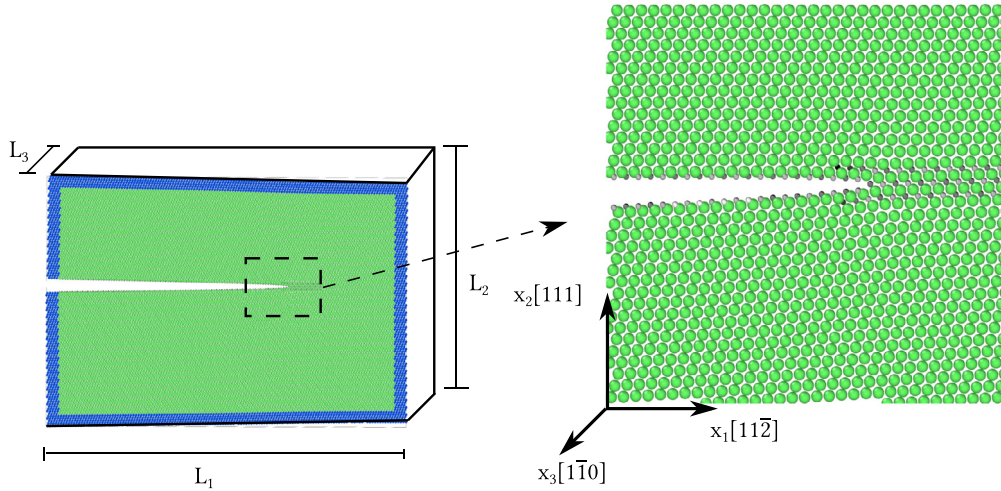


**Fig. B1.** Simulation cell used for the NEB and fracture calculations. Blue: Ni atoms on the boundary that are held fixed to the imposed displacement; Green: Ni atoms that are not fixed during the simulations; Gray: Hydrogen atoms with gray scale indicating the  $x_3$  (out-of-plane) coordinate. (For interpretation of the references to color in this figure legend, the reader is referred to the web version of this article.)

Thus

$$\begin{aligned}\gamma^{\text{fr}} &= \gamma_0^{\text{fr}} + \frac{T \Delta S}{A} \\ &= \gamma_0^{\text{fr}} + \frac{2k_B T}{A_0} \{ (1 - c_s) \ln(1 - c_s) + c_s \ln c_s \\ &\quad + (1 - c_{ss}) \ln(1 - c_{ss}) + c_{ss} \ln c_{ss} - (c_s + c_{ss}) \ln c_b \} \quad (\text{A.9})\end{aligned}$$

## Appendix B. Methods

Spin-polarized first-principles calculations use density functional theory (DFT) as implemented in the Vienna *Ab initio* simulation package (VASP) [48,49] based on projected augmented waves method (PAW). The electron exchange and correlation functionals were described by the generalized gradient approximation (GGA) with Perdew-Burke-Ernzerhof (PBE) format [50]. The cut-off energy for bulk Ni is 600 eV with a Monkhorst-Pack [51]  $k$ -point grid of  $18 \times 18 \times 18$  and first-order Methfessel-Paxton [52] smearing scheme with 0.1 eV. (111) surfaces were constructed a 12 Å vacuum region inserted to create the free (111) surfaces. The bottom three (111) layers were fixed while all other atoms could relax freely. Here, we use a cut-off energy of 380 eV and a  $6 \times 8 \times 1$  Monkhorst-Pack  $k$ -point grid. In all cases, convergence in structural optimization for energy and atomic force was set to  $10^{-6}$  eV and  $10^{-3}$  eV/Å, respectively.

The molecular statics and NEB simulations are performed using the Large-scale Atomic/Molecular Massively Parallel Simulator (LAMMPS) [53] and atomic configurations are visualized using the Open Visualization Tool (OVITO) [54]. The simulation cell size is  $l_1 \times l_2 \times l_3 = 420 \text{ Å} \times 490 \text{ Å} \times 4.96 \text{ Å}$  containing a three-layer hydride along the central plane  $x_2 = 0$  as shown in Fig. B.9. We insert a sharp (111)[110] crack by deleting atomic interactions across the crack faces. We fully saturate the binding sites of the crack faces with hydrogen atoms with the same procedure as given in ref. [55]. For fracture simulations, a K-load is applied by displacing the atoms within the specimen due to the displacement field of a semi-infinite crack in an anisotropic elastic body and then fixing boundary atoms. The system is then relaxed by a conjugate gradient method. The atomic interaction use a new EAM potential adapted from previous versions [27,35] (Appendix C).

For the nudged elastic band (NEB) calculation [56], the initial state is as described above. The final state is constructed by advancing the crack by  $a/\sqrt{2} = 2.48 \text{ Å}$  and displacing 50% of the

subsurface H atoms to the newly formed crack surface (see Figs. 3b and Fig. 3c).

## Appendix C. Validated Ni–H interatomic potential

The fracture problems cannot be simulated by the DFT method due to the high computational cost. Here we adapt a previous Ni–H EAM potential to reproduce the results of the DFT calculations given in Section 2 of this paper.

The potential was originally fitted by Angelo et al. [35,57], and modified by Song and Curtin [27]. Another modification of this potential was used by Tehranchi and Curtin [55]. Here, we have changed the parameters of this potential further and slightly modified the functional form of the Ni–H pair interaction to reproduce the key DFT values controlling the fracture process. The new parameters are given in Table C.1. The functional form of the Ni–H pair potentials is now changed to

$$\phi(r) = \begin{cases} c_1 e^{\frac{1}{r-r_{\text{CH}}}} (e^{-2c_2(-c_3+r)} - 2e^{-c_2(-c_3+r)}) \\ \quad + c_{10\text{Ni}} c_{4\text{Ni}} e^{\frac{1}{r-r_{\text{cNi}}}} (2^9 e^{2c_{5\text{Ni}} r} + e^{-c_{5\text{Ni}} r}) r^6 \\ \quad + c_{10\text{H}} c_{4\text{H}} e^{\frac{1}{r-r_{\text{CH}}}} (2^9 e^{-2c_{5\text{H}} r} + e^{-c_{5\text{H}} r}) r^6 & 0 \leq r \leq r_{\text{CH}} \\ c_{10\text{Ni}} c_{4\text{Ni}} e^{\frac{1}{(r-r_{\text{cNi}})^2}} (2^9 e^{-2c_{5\text{Ni}} r} + e^{-c_{5\text{Ni}} r}) r^6 \\ \quad + \delta e^{\frac{-(r-r_{\text{CH}})^2}{20}} & r_{\text{CH}} \leq r \leq r_{\text{cNi}} \\ 0 & r \geq r_{\text{cNi}} \end{cases} \quad (\text{C.1})$$

where

$$\delta = c_{10\text{Ni}} c_{4\text{Ni}} (e^{\frac{1}{r_{\text{CH}}-r_{\text{cNi}}}} - e^{\frac{1}{(r_{\text{CH}}-r_{\text{cNi}})^2}}) (2^9 e^{-2r_{\text{cNi}} r_{\text{CH}}} + e^{-c_{5\text{Ni}} r_{\text{CH}}}) r_{\text{CH}}^6 \quad (\text{C.2})$$

Table C.2 shows the (111) surface energy versus surface coverage as predicted by the adapted EAM potential and as computed

**Table C1**

Original and modified parameters for the Ni–H EAM potential based on the formulation of [35,57]. Also shown are relevant properties of bulk Ni, as predicted by the potential.

parameter	original [35,57]	modified
$c_{10}^{\text{H}} (\text{eV})$	13.26	12.8
$c_9$	1.1292331	1.1092331
$r_c^{\text{H}} (\text{Å})$	2.8	2.3



**Table E1**

Minimum fracture energies and associated critical stress intensity factors for cleavage  $K_{Ic}$  and emission  $K_{Ie}$  for various symmetric tilt grain boundaries with tilt axis of  $\langle 110 \rangle$  in Ni in the absence of H, with full segregation of H at  $T=0$  K, with full segregation of H at  $T=0$  K and local diffusion to the fracture surface, and for fully-H-saturated fracture surfaces due to aggregation ahead of a crack tip. Cases where  $K_{Ic} < K_{Ie}$  are highlighted in bold and only occur when local diffusion is permitted.

GB	No H			All GB sites occupied		All GB sites occupied +local diffusion		All GB surface sites occupied	
	$K_{Ie}$ (MPa $\sqrt{m}$ )	$\gamma^{fr}$ (J/m <sup>2</sup> )	$K_{Ic}$ (MPa $\sqrt{m}$ )	$\gamma^{fr}$ (J/m <sup>2</sup> )	$K_{Ic}$ (MPa $\sqrt{m}$ )	$\gamma^{fr}$ (J/m <sup>2</sup> )	$K_{Ic}$ (MPa $\sqrt{m}$ )	$\gamma^{fr}$ (J/m <sup>2</sup> )	$K_{Ic}$ (MPa $\sqrt{m}$ )
Ni $\Sigma$ 19(331)	0.70	3.59	1.00	2.14	0.87	1.75	0.70	−0.46	<b>0.00</b>
Ni $\Sigma$ 27(115)	0.61	3.44	1.00	3.21	0.96	2.94	0.92	0.43	<b>0.35</b>
Ni $\Sigma$ 33(441)	0.72	3.40	0.98	2.62	0.87	2.41	0.83	0.72	<b>0.45</b>
Ni $\Sigma$ 33(554)	0.64	3.31	0.95	2.61	0.84	2.41	0.81	0.82	<b>0.47</b>
Ni $\Sigma$ 41(443)	0.67	3.24	0.97	2.51	0.85	2.21	0.80	0.90	<b>0.51</b>
Ni $\Sigma$ 99(557)	0.62	3.27	1.00	3.12	0.98	3.07	0.97	−0.15	<b>0.00</b>

grain boundaries and free surfaces, we can anticipate that the fracture energy, which involves the difference between the latter two energies, involves some cancellation of the errors in those two energies.

## References

- [1] R.L.S. Thomas, J.R. Scully, R.P. Gangloff, Internal hydrogen embrittlement of ultrahigh-strength aermet 100 steel, *Metall. Mater. Trans. A* 34 (2) (2003) 327–344.
- [2] S. Bechtle, M. Kumar, B.P. Somerday, M.E. Launey, R.O. Ritchie, Grain-boundary engineering markedly reduces susceptibility to intergranular hydrogen embrittlement in metallic materials, *Acta Mater.* 57 (14) (2009) 4148–4157.
- [3] D. Lassila, H. Birnbaum, The effect of diffusive hydrogen segregation on fracture of polycrystalline nickel, *Acta Metall.* 34 (7) (1986) 1237–1243.
- [4] Y. Lee, R.P. Gangloff, Measurement and modeling of hydrogen environment-assisted cracking of ultra-high-strength steel, *Metall. Mater. Trans. A* 38 A (13) (2007) 2174–2190.
- [5] R.P. Gangloff, Hydrogen-assisted cracking, *Compr. Struct. Integr.* 6 (2007) 31–101.
- [6] W.H. Johnson, On some remarkable changes produced in iron and steels by the action of hydrogen acids, *Proc. Royal Soc. Lond.* 23 (1875) 168–175.
- [7] A.E.R. Troiano, The role of hydrogen and other interstitials in the mechanical behavior of metals, *Trans. ASM* 52 (1) (1960) 54–80.
- [8] W. Gerberich, P. Marsh, J. Hoehn, S. Venkataraman, H. Huang, Hydrogen/plasticity interactions in stress corrosion cracking, in: *Proceedings of the Corrosion-Deformation Interactions (CDI'92)*, Les Editions de Physique, Les Ulis, 1993, pp. 325–353.
- [9] R. Oriani, P. Josephic, Equilibrium aspects of hydrogen-induced cracking of steels, *Acta Metall.* 22 (9) (1974) 1065–1074.
- [10] W. Gerberich, T.J. Foecke, in: *Hydrogen Enhanced Decohesion in Fe-Si Single Crystals: Implications to Modeling of Thresholds Hydrogen Effects on Materials Behavior*, (TMS), Warrendale, PA, 1990, pp. 687–701, editors.
- [11] R. Oriani, A mechanistic theory of hydrogen embrittlement of steels, *Berichte der Bunsengesellschaft für physikalische Chemie* 76 (8) (1972) 848–857.
- [12] W.W. Gerberich, P.G. Marsh, J.W. Hoehn, Hydrogen induced cracking mechanisms – are there critical experiments? in: *Proceedings of the Hydrogen Effects in Materials*, 1996, pp. 539–551.
- [13] J. Song, M. Soare, W. Curtin, Testing continuum concepts for hydrogen embrittlement in metals using atomistics, *Modell. Simul. Mater. Sci. Eng.* 18 (4) (2010) 045003.
- [14] R. Kirchheim, B. Somerday, P. Sofronis, Chemomechanical effects on the separation of interfaces occurring during fracture with emphasis on the hydrogen-iron and hydrogen-nickel system, *Acta Mater.* 99 (2015) 87–98.
- [15] D.P. Abraham, C.J. Al tsetter, Hydrogen-enhanced localization of plasticity in an austenitic stainless steel, *Metall. Mater. Trans. A* 26 (11) (1995) 2859–2871.
- [16] Y. Murakami, The Effect of Hydrogen on Fatigue Properties of Metals Used for Fuel Cell System, in: *Advances in Fracture Research*, Springer, 2006, pp. 167–195.
- [17] C.D. Beachem, New model for hydrogen-assisted cracking (hydrogen embrittlement), *Metall. Trans.* 3 (2) (1972) 437–451.
- [18] H.K. Birnbaum, P. Sofronis, Hydrogen-enhanced localized plasticity a mechanism for hydrogen-related fracture, *Mater. Sci. Eng.: A* 176 (1) (1994) 191–202.
- [19] I. Robertson, The effect of hydrogen on dislocation dynamics, *Eng. Fract. Mech.* 68 (6) (2001) 671–692.
- [20] S. Li, Y. Li, Y.-C. Lo, T. Neeraj, R. Srinivasan, X. Ding, J. Sun, L. Qi, P. Gumbsch, J. Li, The interaction of dislocations and hydrogen-vacancy complexes and its importance for deformation-induced proto nano-voids formation in  $\alpha$ -Fe, *Int. J. Plast.* 74 (2015) 175–191.
- [21] S.K. Lawrence, Y. Yagodzinsky, H. Hänninen, E. Korhonen, F. Tuomisto, Z.D. Harris, B.P. Somerday, Effects of grain size and deformation temperature on hydrogen-enhanced vacancy formation in ni alloys, *Acta Mater.* 128 (2017) 218–226.
- [22] Z.D. Harris, S.K. Lawrence, D.L. Medlin, G. Guetard, J.T. Burns, B.P. Somerday, Elucidating the contribution of mobile hydrogen-deformation interactions to hydrogen-induced intergranular cracking in polycrystalline nickel, *Acta Mater.* 158 (2018) 180–192.
- [23] T. Neeraj, R. Srinivasan, J. Li, Hydrogen embrittlement of ferritic steels: observations on deformation microstructure, nanoscale dimples and failure by nanovoiding, *Acta Mater.* 60 (13) (2012) 5160–5171.
- [24] R. Nazarov, T. Hickel, J. Neugebauer, First-principles study of the thermodynamics of hydrogen-vacancy interaction in FCC iron, *Phys. Rev. B* 82 (22) (2010) 224104.
- [25] D. Tanguy, Y. Wang, D. Connétable, Stability of vacancy-hydrogen clusters in nickel from first-principles calculations, *Acta Mater.* 78 (2014) 135–143.
- [26] A. Tehranchi, X. Zhang, G. Lu, W.A. Curtin, Hydrogen-vacancy-dislocation interactions in  $\alpha$ -Fe, *Modell. Simul. Mater. Sci. Eng.* 25 (2) (2016) 025001.
- [27] J. Song, W.A. Curtin, A nanoscale mechanism of hydrogen embrittlement in metals, *Acta Mater.* 59 (4) (2011) 1557–1569.
- [28] J. Song, W. Curtin, Atomic mechanism and prediction of hydrogen embrittlement in iron, *Nat Mater.* 12 (2) (2013) 145–151.
- [29] I.M. Robertson, P. Sofronis, A. Nagao, M. Martin, S. Wang, D. Gross, K. Nygren, Hydrogen embrittlement understood, *Metall. Mater. Trans. A* 46 (6) (2015) 2323–2341.
- [30] B. Kuhr, D. Farkas, I.M. Robertson, Atomistic studies of hydrogen effects on grain boundary structure and deformation response in FCC ni, *Comput. Mater. Sci.* 122 (2016) 92–101.
- [31] A.A.A. Griffith, M. Eng, Vi. the phenomena of rupture and flow in solids, *Phil. Trans. R. Soc. Lond. A* 221 (582–593) (1921) 163–198.
- [32] J.R. Rice, Dislocation nucleation from a crack tip: an analysis based on the Peierls concept, *J. Mech. Phys. Solids* 40 (2) (1992) 239–271.
- [33] P. Andric, W. Curtin, New theory for mode I crack-tip dislocation emission, *J. Mech. Phys. Solids* 106 (2017) 315–337.
- [34] J. Rice, An examination of the fracture mechanics energy balance from the point of view of continuum mechanics, in: *Proceedings of the ICF1, Japan 1965*, 1965.
- [35] J.E. Angelo, N.R. Moody, M.I. Baskes, Trapping of hydrogen to lattice defects in nickel, *Modell. Simul. Mater. Sci. Eng.* 3 (3) (1995) 289.
- [36] Y. Mishin, D. Farkas, M. Mehl, D. Papaconstantopoulos, Interatomic potentials for monoatomic metals from experimental data and ab initio calculations, *Phys. Rev. B* 59 (5) (1999) 3393.
- [37] D.H. Warner, W. Curtin, Origins and implications of temperature-dependent activation energy barriers for dislocation nucleation in face-centered cubic metals, *Acta Mater.* 57 (14) (2009) 4267–4277.
- [38] J.A. Zimmerman, H. Gao, F.F. Abraham, Generalized stacking fault energies for embedded atom FCC metals, *Modell. Simul. Mater. Sci. Eng.* 8 (2) (2000) 103.
- [39] J. von Pezold, L. Lymperakis, J. Neugebauer, Hydrogen-enhanced local plasticity at dilute bulk h concentrations: the role of h-h interactions and the formation of local hydrides, *Acta Mater.* 59 (8) (2011) 2969–2980.
- [40] E. Martínez-Pañeda, C.F. Niordson, R.P. Gangloff, Strain gradient plasticity-based modeling of hydrogen environment assisted cracking, *Acta Mater.* 117 (2016) 321–332.
- [41] A. Tehranchi, W.A. Curtin, Atomistic study of Hydrogen embrittlement of grain boundaries in Nickel: I. Fracture, *J. Mech. Phys. Solids* 101 (2017) 150–165.
- [42] D. Di Stefano, M. Mrovec, C. Elsässer, First-principles investigation of quantum mechanical effects on the diffusion of hydrogen in iron and nickel, *Phys. Rev. B* 92 (22) (2015) 224301.
- [43] X. Zhou, N. Mousseau, J. Song, Is hydrogen diffusion along grain boundaries fast or slow? Atomistic origin and mechanistic modeling, *Phys. Rev. Lett.* 122 (21) (2019) 215501.
- [44] H. Luo, W. Lu, X. Fang, D. Ponge, Z. Li, D. Raabe, Beating hydrogen with its own weapon: nano-twin gradients enhance embrittlement resistance of a high-entropy alloy, *Mater. Today* 21 (10) (2018) 1003–1009.
- [45] H. Luo, Z. Li, W. Lu, D. Ponge, D. Raabe, Hydrogen embrittlement of an interstitial equimolar high-entropy alloy, *Corros. Sci.* 136 (2018) 403–408.
- [46] H. Luo, Z. Li, D. Raabe, Hydrogen enhances strength and ductility of an equiatomic high-entropy alloy, *Sci. Rep.* 7 (1) (2017) 9892.

- [47] K. Nygren, K. Bertsch, S. Wang, H. Bei, A. Nagao, I. Robertson, Hydrogen embrittlement in compositionally complex FeNiCoCrMn fcc solid solution alloy, *Curr. Opin. Solid State Mater. Sci.* 22 (1) (2018) 1–7.
- [48] G. Kresse, J. Furthmüller, Efficient iterative schemes for ab initio total-energy calculations using a plane-wave basis set, *Phys. Rev. B* 54 (16) (1996) 11169.
- [49] G. Kresse, From ultrasoft pseudopotentials to the projector augmented-wave method, *Phys. Rev. B* 59 (3) (1999) 1758–1775.
- [50] J.P. Perdew, K. Burke, M. Ernzerhof, Generalized gradient approximation made simple, *Phys. Rev. Lett.* 77 (18) (1996) 3865.
- [51] H.J. Monkhorst, J.D. Pack, Special points for Brillouin-zone integrations, *Phys. Rev. B* 13 (12) (1976) 5188.
- [52] M. Methfessel, A.T. Paxton, High-precision sampling for Brillouin-zone integration in metals, *Phys. Rev. B* 40 (6) (1989) 3616–3621.
- [53] S. Plimpton, Fast parallel algorithms for short-range molecular dynamics, *J. Comput. Phys.* 117 (1) (1995) 1–19.
- [54] A.e. Stukowski, Visualization and analysis of atomistic simulation data with Ovito—the open visualization tool, *Modell. Simul. Mater. Sci. Eng.* 18 (1) (2009) 015012.
- [55] A.i. Tehranchi, W.A. Curtin, Atomistic study of hydrogen embrittlement of grain boundaries in nickel: I. fracture, *J. Mech. Phys. Solids* (2017).
- [56] G. Henkelman, B.P. Uberuaga, H. Jónsson, A climbing image nudged elastic band method for finding saddle points and minimum energy paths, *J. Chem. Phys.* 113 (22) (2000) 9901–9904.
- [57] M. Baskes, X. Sha, J. Angelo, N. Moody, Trapping of hydrogen to lattice defects in nickel, *Modell. Simul. Mater. Sci. Eng.* 5 (6) (1997) 651.
- [58] X. Zhou, D. Marchand, D.L. McDowell, T. Zhu, J. Song, Chemomechanical origin of hydrogen trapping at grain boundaries in FCC metals, *Phys. Rev. Lett.* 116 (7) (2016) 075502.